The Astrophysical Journal, 523:432–443, 1999 September 20

EMISSION MEASURE DISTRIBUTION FOR AN ACTIVE REGION USING COORDINATED SERTS AND *YOHKOH* SXT OBSERVATIONS

J. T. Schmelz,[1] J. L. R. Saba,[2] K. T. Strong,[3] H. D. Winter,[1] and J. W. Brosius[4]
Received 1999 March 16; accepted 1999 May 13

ABSTRACT

Often the derived temperature of an active region reflects the method and the nature of the instrument used in its measurement. The emission measure (i.e., the amount of emitting material) derived from spectroscopic observations usually depends on assumptions about the absolute elemental abundances and ionization fractions of the emitting ions. Yet establishing the distribution of emission measure with temperature is the first step needed to proceed with most of the interesting physics of active regions—including heating processes, cooling timescales, and loop stability. Accurately characterizing the thermal distribution of the coronal plasma requires data which can resolve multithermal features and constrain both low- and high-temperature emission. To model the temperature distribution of NOAA Active Region 7563, we have combined broadband filter data from the *Yohkoh* Soft X-Ray Telescope (SXT) with simultaneous spectral line data from the Goddard Solar EUV Rocket Telescope and Spectrograph (SERTS) taken during its flight on 1993 August 17. We have used a forward-folding technique to determine the emission measure distribution of the active region loops. We have found that (1) the SXT response functions are sensitive to both the elemental abundances and the ionization fractions assumed to compute the solar spectrum that is folded through the instrument effective area; (2) the relative calibration between the SERTS and the SXT instruments must be adjusted by a factor of 2 (a value consistent with the absolute measurement uncertainty of the 1993 SERTS flight) no matter which abundances or iron ionization fractions are used; (3) the two-peaked differential emission measure previously determined using SERTS data alone is not consistent with the SXT data: including the SXT data as a high-temperature constraint in the analysis requires that the emission above about 3 MK drop off steeply rather than extending out to 6 MK. The sensitivity of the SXT filter response functions to elemental abundance and iron ionization fraction could have a major impact on many routine analyses of SXT data. The emission measures can be greatly affected (up to a factor of 7) and temperatures derived from filter ratios can be significantly altered (up to at least 40%) by adopting different sets of commonly used elemental and ionic abundances. The results of our multithermal analysis imply that using broadband SXT data or a comparable high-temperature constraint in conjunction with high-resolution spectra covering a wide lower temperature range to study solar active regions can significantly improve the information derived from either data set alone. In this study, the revised multithermal distribution reduces the thermal energy content of the region by about a factor of 2 and the required heating by about a factor of 5, which in turn relaxes some constraints on possible heating models.

Subject headings: Sun: activity — Sun: X-rays, gamma rays

1. INTRODUCTION

Understanding features and phenomena on the Sun requires knowledge of the basic plasma parameters, such as composition, temperature, emission measure, electron density, filling factors, and their distributions. These quantities are important inputs for many different kinds of solar physics problems. For example, they enter into calculations of radiative losses and conductive cooling in coronal structures and in estimates of coronal loop stability; they are used to define the energy balance and heating requirements of a region, which in turn provide constraints on possible coronal heating mechanisms; they are used to constrain possible coronal emission mechanisms in different wave bands (e.g., radio and X-ray; Schmelz et al. 1994) and, hence, the coronal magnetic field; they are used to characterize the thermal distribution of coronal structures and yield improved understanding of the source regions for solar energetic particles, whose "frozen-in" temperatures reflect the conditions where the source material was still in closed loops and dense enough to be collisional.

Yohkoh Soft X-Ray Telescope (SXT) broadband filter data were acquired in coincidence with high-resolution EUV spectral line data taken during the 1993 flight of the Goddard Solar EUV Rocket Telescope and Spectrograph (SERTS). A joint analysis of plasma parameter measurements obtained from these data provides an extraordinary opportunity to combine the powerful plasma diagnostic capability of high-resolution EUV spectra with simultaneous higher temperature coronal images of exceptional quality to explore the physics of some of the fundamental structures in the solar atmosphere. The jointly observed features include both quiet-Sun and active region loops. We focus here on the active region data.

Individually, the SXT and SERTS data sets represent the state of the art for measurements of their kind. SERTS provides snapshots of the active region loops at many differ-

[1] University of Memphis, Physics Department, Memphis, TN 38152.
[2] Lockheed Martin Solar and Astrophysics Laboratory, stationed at NASA/GSFC, Code 682, Greenbelt, MD 20771.
[3] Lockheed Martin Solar and Astrophysics Laboratory, 3251 Hanover Street, Palo Alto, CA 94304.
[4] Raytheon ITSS, stationed at NASA/GSFC, Code 682, Greenbelt, MD 20771.

ent temperatures (0.05–3 MK), as well as detailed information on their temperature and density distributions, composition, and line-of-sight motions. SXT provides cotemporal images of the high-temperature corona (>2 MK) and monitors temporal evolution of the target structures before, during, and after the SERTS flight. These images can help identify structures in stages of cooling or heating which might be neglected or misinterpreted from the short-duration SERTS data alone; they also provide information on the large-scale environment and associated structures outside the SERTS field of view. The baseline and cadence, spatial resolution and low scatter, sensitivity, and dynamic range of the SXT images combine to make an unparalleled set of broadband coronal images. Together, the SXT and SERTS data provide complementary constraints on the physical conditions of coronal structures—information which is essential for realistic models of those structures and the physics which governs them.

Brosius et al. (1996, 1997) computed the temperatures, emission measures, and line-ratio densities from the 1993 SERTS data using spectral line analysis and compared the temperatures with those derived from *Yohkoh* SXT filter ratios. (Broadband filter ratios, currently widely used in *Yohkoh* analysis, often give different temperatures from those obtained from spectral line analysis.) They also constructed a differential emission measure (DEM) distribution for the active region plasma using the SERTS data alone. In this paper, we use the combined SERTS and *Yohkoh* SXT information to produce a consistent multithermal picture of the active region loops.

2. OBSERVATIONS

For this study, we concentrate on comparison and joint analysis of the simultaneous SERTS and SXT data obtained on 1993 August 17. Both instruments observed NOAA Active Region 7563, whose solar coordinates at 1800 UT were S10° E09°. This analysis is limited to a 2′.7 (37 SERTS pixels) by 4″.4 (1 SERTS pixel) slice through the central portion of the active region. SXT images before, during, and after the SERTS flight are also examined to monitor potential temporal variability.

2.1. *SERTS Observations*

The SERTS imaging spectrograph is described by Neupert et al. (1992). The spectrograph entrance aperture was designed so that both spectra and spectroheliograms could be obtained simultaneously—spectra are obtained along a narrow 4′.9 long slit (i.e., 64″ × 4″.4) connecting two 5′ × 8′ rectangular lobes within which the spectroheliograms are imaged. The spectral resolution is ~ 55 mÅ.

SERTS was launched from White Sands, New Mexico, on 1993 August 17 at 18:00 UT. It reached a maximum altitude of about 320 km and acquired spectrographic data between 235 and 450 Å for about 7 minutes. Relative line intensities are accurate to better than 20% at wavelengths above 300 Å and are somewhat worse at wavelengths below 300 Å. Brosius et al. (1996) list the EUV emission lines observed in the averaged active region spectrum. Brosius, Davila, & Thomas (1998) give details of the SERTS calibration procedures and find that the absolute photometric scale is accurate to about a factor of 2. The SERTS spectroheliograms and slit spectra were co-aligned with ground-based observations by matching features common to both the SERTS He II 304 Å images and Kitt Peak He I 10830 Å images.

2.2. *Yohkoh SXT Observations*

The *Yohkoh* SXT images are taken in broadband soft X-rays (approximately 2–60 Å) and hence are entirely coronal. Although broadband filter combinations are less powerful for detailed multithermal plasma diagnostic measurements than are high-resolution spectra, a rich array of new results from the SXT has been obtained on the physics of phenomena as wide ranging as coronal bright points, active regions, flares, coronal mass ejections, and large-scale coronal structures. Details of the SXT instrument and operation modes can be obtained from the prelaunch paper by Tsuneta et al. (1991) and the more recent *Yohkoh* Analysis Guide (Morrison 1994). The latter reference also documents much of the available *Yohkoh* software for data reduction and analysis.

SXT provided cotemporal high-temperature (>2 MK) images of the targeted structures and the spatial context of large-scale or interacting structures extending beyond the SERTS field of view. It also monitored variability in the structures before, during, and after the SERTS flight. Although the coverage was not uniform in cadence, the sampling was sufficient to identify transient heating episodes or loop cooling which might have affected the thermal analysis of the joint data. None was observed. (As shown in § 4.2, the fastest relevant cooling timescale is expected to be about 10^3 s.) Over the period from 2 hr before to 2 hr after the SERTS flight, SXT took a series of 45 individual full-disk images, alternating between the thin Al and AlMgMn filters, in sets of three exposures each (to make 15 "composite images" in which most features are well exposed). In addition, SXT took "partial frame" high-resolution (2″.455 pixel) images in three filters (thin Al, AlMgMn, and thick Al), with pointing alternating between the SERTS target region and a brighter region on the limb which was outside the SERTS field of view. The SERTS region was sampled with 18 images from 16:10 to 17:05 UT, 21 images from 17:50 to 18:12 UT, and 31 images from 19:27 to 20:19 UT. Only SXT images from the second period, from 10 minutes before to 2 minutes after the SERTS flight, were used in the joint SERTS/SXT multithermal analysis discussed below. The last set of images showed that a small brightening occurred adjacent to the subfield of interest, about 90 minutes after the SERTS flight. However, there were no significant changes in intensity or morphology in the target subfield during the SERTS flight or the preceding hour which would impact the analysis herein. In particular, most of the SXT images were taken in the thin Al or AlMgMn filters, which are quite sensitive to plasma temperatures at which Fe XVII is formed (see § 4.1).

3. ANALYSIS

Taken individually, either the SERTS or the SXT data can be misleading if assumed to represent the total picture. The SXT broadband filter data are dominated by the hottest plasma in the field of view because the SXT response functions peak at temperatures much greater than typical active region plasma temperatures. This means that any SXT isothermal estimate of the "mean" temperature of a distribution will convolve the high-temperature sensitivity of the filter response with the actual emission measure distribution both along the line of sight and across the field of view. Thus it can give an answer that is artificially weighted toward a hotter value than the true mean temperature. Using a combination of several of the available filter ratios does not necessarily overcome this difficulty because of statistical and systematic uncertainties.

The hottest temperature lines observed in the SERTS spectrum of AR 7563 were a pair of relatively weak Fe XVII lines at 347.82 and 350.52 Å. The peak response of these lines occurs at about log $T = 6.45$ (Arnaud & Rothenflug 1985) or 6.6 (Arnaud & Raymond 1992), so that the available SERTS data do not constrain the higher temperature active region plasma. Although the SERTS wavelength range does include higher temperature lines, none of these were detected for this active region. Because of the shortness of the exposures, the signal-to-noise level was not adequate to use the absence of the lines to constrain the amount of high-temperature plasma.

Historically, temperature measurements by two instruments with different temperature responses give different answers. Usually an "effective temperature" is derived in an isothermal approximation while it is likely in practice that there is a distribution of temperatures from structures along the line of sight and unresolved features across the field of view. Only an instrument, or combination of instruments, with good temperature coverage between 1 and 10 MK can adequately characterize the thermal distribution of coronal plasma in active regions. Although the majority of the SERTS emission lines have a significantly cooler temperature response than that of the dominant SXT response, there is sufficient overlap of the temperature responses to permit self-consistency checks between the SERTS and SXT analyses. Therefore, it is possible to use the combined data set to broaden the temperature range for accurate multithermal analysis of active region data; the SXT data are used in particular to constrain the high-temperature end of the emission measure distribution which is typically poorly defined in studies using EUV data alone.

Brosius et al. (1996) published a DEM curve of the active region plasma using the SERTS spectral data alone. DEM is a standard multithermal analysis technique. Various implementations of the DEM method were tested and compared with good results in a major project planning for analysis of data from UV and EUV spectrometers on the *Solar and Heliospheric Observatory* (*SOHO*). From this study (see Harrison & Thompson 1991), the specific program and procedure of the Arcetri DEM code of Monsignori-Fossi and Landini—used to produce the DEM curves published by Brosius et al. (1996)—are known to be accurate and were readily accessible when that analysis was done. The DEM distribution for the active region (see their Fig. 8) was double peaked, but the higher temperature ($\sim$4 MK) component at the extreme end of the SERTS range of sensitivity was poorly constrained. The shallow dip between the peaks, combined with the relatively large measurement uncertainty for the few available high-temperature lines, suggests that the derived double peak may not be significant. The higher temperature response of SXT can be used to test the reality of the apparent double-peaked structure of the SERTS active region DEM curve as we discuss in § 3.4.

3.1. *Elemental Abundance Normalization*

Before the SXT and SERTS results can be compared with confidence, the underlying assumptions used for the analysis of data from each instrument should first be reconciled. The SXT response functions are computed by folding a synthetic solar spectrum through the measured effective area for each of the five different filters. The current "default" synthetic spectrum used in SXT analysis assumes the set of "adopted coronal" abundances published by Meyer (1985), where the abundances of elements with high first ionization potential (FIP) are depleted in the corona with respect to their photospheric values by about a factor of 4 and the abundances of low-FIP elements are the same in the corona and the photosphere. The resulting response functions are published in the *Yohkoh* Analysis Guide (Morrison 1994) and are used in all of the routine SXT analysis software.

Unfortunately, the normalization of the coronal trace elemental abundances with respect to hydrogen is not well known. A competing empirical model of coronal composition has low-FIP elements enhanced by about a factor of 4 with respect to their photospheric values and high-FIP elements the same in the corona and the photosphere (Feldman 1992); that is, there is about a factor of 4 difference in the overall coronal abundances relative to hydrogen between the two models. The latter model was used in producing the DEM curves published by Brosius et al. (1996). The absolute elemental abundances, i.e., abundances relative to hydrogen, affect the normalization of the emission measure, while relative abundances of different heavy elements affect the shape of the DEM distribution.

Since neither SXT nor SERTS provides any direct information on abundance normalization (and hence on absolute emission measures), we consider results published elsewhere. Recently, Schmelz & Fludra (1998) analyzed data for 93 flares observed with the *Yohkoh* Bragg Crystal Spectrometer and derived absolute coronal abundances for sulfur, calcium, and iron. The mean *Yohkoh* abundance of intermediate-FIP sulfur relative to hydrogen is smaller than the photospheric value by over a factor of 2. The mean abundance of low-FIP calcium is about 50% greater than the photospheric value. The mean abundance of low-FIP iron shows greater scatter around its mean value but is still about a factor of about 1.5 higher than the accepted photospheric value. These results were not consistent with either of the two empirical abundance normalization models (Feldman 1992; Meyer 1985) discussed above. They combined these values with all known absolute abundance measurements published in the literature for many events—from 25 to several hundred—for both spectroscopic and solar energetic particle results. These data agree with the results from *Yohkoh*—neither of the two most commonly used empirical models accurately describes the majority of the absolute abundance measurements.

The available data are better represented by the set of "hybrid" coronal abundances where there is *both* an enhancement of low-FIP abundances *and* a depletion of high-FIP abundances, each by about a factor of 2 compared with their photospheric values relative to hydrogen. These hybrid abundances are listed in Table 1. Although excellent examples of abundance variability can be found in the literature, this hybrid abundance set appears to be the best way to characterize the mean composition in the near corona. In the absence of other specific contrary information for a given data set, the hybrid set also has the virtue of splitting the difference between the extremes of the two more common models, thereby cutting the normalization uncer-

TABLE 1

HYBRID ABUNDANCES

Element	FIP (eV)	Photospheric Abundance	Hybrid Abundance	Hybrid/Photospheric
K	4.32	1.33E−07	2.79E−07	2.10
Na	5.12	2.03E−06	4.25E−06	2.10
Al	5.96	3.00E−06	6.30E−06	2.10
Ca	6.09	2.16E−06	4.54E−06	2.10
Cr.......	6.74	4.77E−07	1.00E−06	2.10
Ti	6.81	8.47E−08	1.78E−07	2.10
Mg......	7.61	3.78E−05	7.94E−05	2.10
Ni.......	7.61	1.74E−06	3.65E−06	2.10
Fe.......	7.83	3.21E−05	6.74E−05	2.10
Si	8.12	3.53E−05	7.42E−05	2.10
Zn	9.36	4.45E−08	8.01E−08	1.80
S	10.3	1.73E−05	2.08E−05	1.20
P	10.9	3.67E−07	2.75E−07	0.75
C........	11.22	3.97E−04	2.57E−04	0.65
Cl	12.95	1.85E−07	1.20E−07	0.65
O	13.55	8.47E−04	5.48E−04	0.65
N	14.48	1.00E−04	6.47E−05	0.65
Ar.......	15.68	3.57E−06	2.31E−06	0.65
Ne	21.47	1.36E−04	8.83E−05	0.65
He	24.46	9.75E−02	6.31E−02	0.65

tainty factor, and hence the emission measure uncertainty, in half. We adopt the Schmelz & Fludra (1998) abundance values in our DEM analysis in § 3.4.

3.2. *Ionization Balance Calculations*

The SXT default synthetic spectrum also incorporates the ionization balance calculations of Arnaud & Rothenflug (1985) for all elements, while the DEM curves published by Brosius et al. (1996) used revised values for the ionization fractions of iron, as given by Arnaud & Raymond (1992). (The Arnaud & Rothenflug values were used for all other elements.) Most EUV spectral line analyses now use these newer results for iron, which corrects a known error in the earlier calculations; however, some existing data sets are much harder to interpret using the newer calculations. (For example, for *Solar Maximum Mission* Flat Crystal Spectrometer active region data, the Fe XVIII/Fe XVII diagnostic line ratio would imply a temperature that is inconsistent with the upper limits of other high-temperature lines.) The temperature sensitivities of certain lines are strongly affected by the ionization balance calculations adopted, as noted above for Fe XVII (which gave the highest temperature lines used in the SERTS DEM analysis and whose soft X-ray lines dominate the SXT thin filter responses at active region temperatures). The ionization fraction calculations strongly affect the DEM results, and, unfortunately, it is not clear that the newer calculations are the final word. Therefore, we have chosen to compare results from the two sets of calculations to see how they each affect the shape of the DEM curve and the consistency of the SERTS and SXT results.

3.3. *SXT Response Functions*

The sensitivity of the SXT response functions in each of the six analysis bands to abundance normalization and ionization fraction is illustrated in Figures 1 and 2. (Note that the *y*-axes of the plots in Fig. 1 are logarithmic and can be compared directly to the standard plots in the *Yohkoh* Analysis Guide; those in Fig. 2 are linear to emphasize the differences obtained with various sets of elemental and ionic abundances). The sets of responses in the four lowest energy filters appear qualitatively quite similar (as do the standard response curves for these filters), although there are some small quantitative differences that allow ratios of counts from various filter combinations to be used to derive "color temperatures"—that is, estimates of the average plasma temperature convolved with the instrument response. The sets of curves for the thick aluminum and the beryllium filters (Figs. 1*e*, 1*f*, 2*e*, and 2*f*) are very different from the others and from each other, so that ratios between the two, or between either and the thin filters, provide more sensitive measures of color temperature in some regimes if there are sufficient counts.

The dotted line in each panel of Figures 1 and 2 shows the instrument response for the continuum only—the contribution from emission lines is ignored, and the synthetic solar continuum spectrum is folded through the SXT effective areas. (The small effect of changing the abundances and ionization fractions on the continuum response is ignored herein.) The lowest solid curve in each panel shows the standard SXT response, in which the Meyer (1985) adopted coronal abundances and the ionization fractions from Arnaud & Rothenflug (1985) are used to generate the synthetic solar spectrum which is then folded through the SXT effective areas. The other solid curves show the respective SXT response functions generated, again with Arnaud & Rothenflug (1985) ionization fractions, but with abundance normalizations 2, 3, or 4 times as great as before, with the highest curve corresponding to the highest abundances (see figure legends). The dashed curves show the corresponding functions generated when the Arnaud & Raymond (1992) ionization fractions are substituted for iron. In general, the latter responses are considerably higher in the range $\log T = 6.2$–6.8, reflecting the differences in the two sets of iron ionization balance calculations in the active region temperature regime and underlining the importance of iron line emission in the thin filter bands. The response curves for the beryllium filter for the two sets of iron ionization fractions are essentially identical, because of the smaller

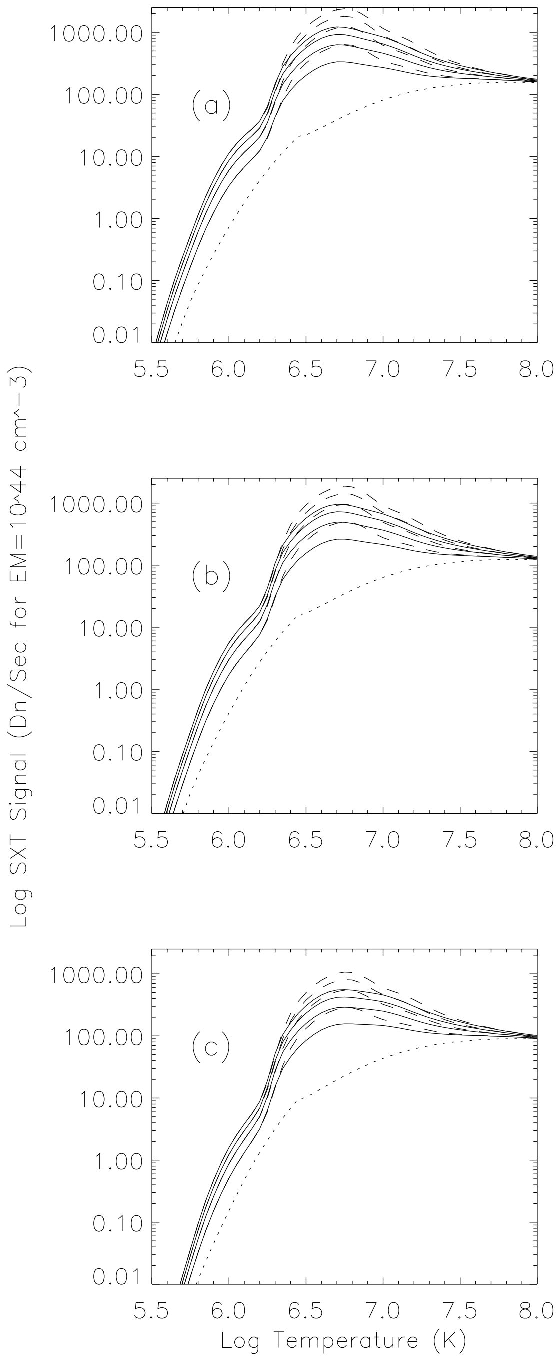

FIG. 1.—SXT response functions for the open filter position, as well as the five SXT analysis filters, generated for the continuum alone (*dotted curve*) and for the continuum plus lines for Arnaud & Rothenflug (1985) ionization fractions (*solid curves*), and with Arnaud & Raymond (1992) ionization fractions substituted for iron (*dashed curves*). The curves in each panel represent the response functions generated for the continuum plus lines assuming (from lowest to highest) adopted coronal abundances from Meyer (1985), 2 times the adopted coronal values (approximating the hybrid abundances of Schmelz & Fludra 1998), 3 times the adopted coronal values, and 4 times the adopted coronal values (approximating the Feldman 1992 abundances). The different panels correspond to the (*a*) open position, (*b*) thin Al filter, (*c*) AlMgMn filter, (*d*) Mg filter, (*e*) thick Al filter, and (*f*) Be filter.

contributions from iron line emission in that band. However, the abundance normalization still makes a significant difference for the beryllium filter response, as it does for the thick aluminum filter response. The abundances and (for all but the beryllium filter) the iron ionization fractions chosen clearly make a significant difference in the SXT filter responses, in contrast to the common expectation that broadband data are insensitive to these assumptions.

Some simple quantitative estimates of the impact of varying these quantities can be made by dividing the adjusted filter response curves for the extreme cases by the standard response curves. Figure 3 shows, for the six analysis bands, several of these adjusted filter responses normalized to the standard SXT response, which is shown here as the solid horizontal line with a value of unity. If the abundance normalization and ionization fractions were unimportant, the ratios of the adjusted curves to the standard curves would approximate straight horizontal lines with values near unity, which they clearly do not. The dashed curves show the responses to the emission lines when the (SXT)

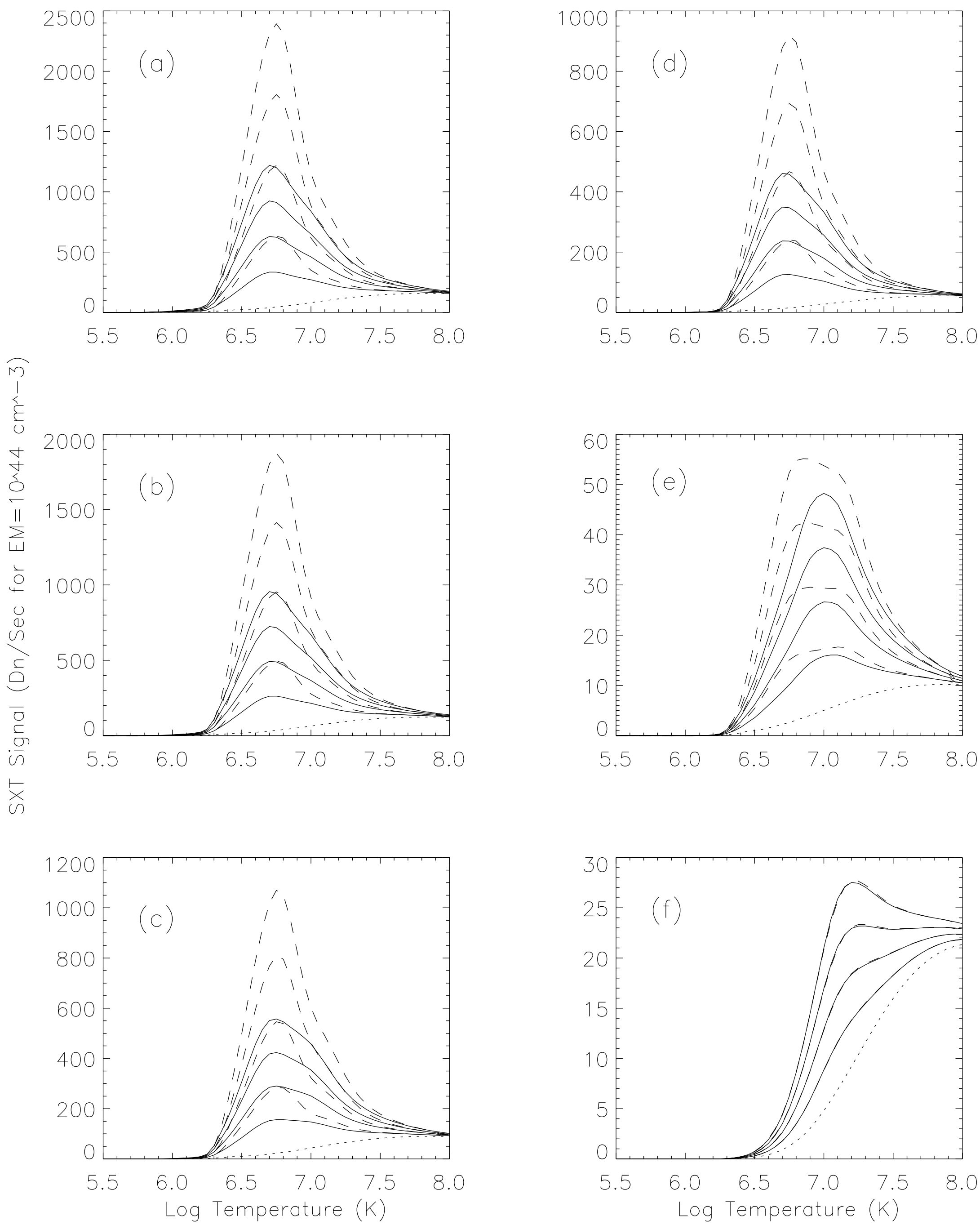

FIG. 2.—Same as Fig. 1, but with the y-axis on a linear scale to show differences more clearly

standard ionization fractions are used but the element abundances are increased by a factor of 4; there is about a factor of 3–3.5 increase in response in the active region regime (although the change is clearly not a constant factor with temperature even in this limited range) except for the beryllium filter, where the factor is about 2–2.5. The dot-dashed curve shows the effect on the filter responses when the (SXT) standard coronal abundances are used but the iron ionization fractions are adjusted; the relative change in the filter response is a strongly varying function of temperature with a peak value of about 2 near log $T = 6.8$. The triple-dot-dashed curve shows the combined change (relative to the standard response) when the maximum abundances we considered and the new iron ionization fractions are used at the same time; the resulting response ratios are a complex function of temperature with peak values as high as 7.1. That is, if one uses Feldman (1992) abundances and Arnaud & Raymond (1992) iron ionization fractions, the SXT responses to active region emission (for all except the beryllium filter) are at least 3 times higher and up to 7 times higher than they are with the usual assumptions used in the SXT analysis software.

Figure 4 shows several filter ratios as a function of temperature, in a format that is familiar from the *Yohkoh* analysis guide. The line-type notation is the same as that for Figure 3. Since the response curves of the low-energy filters have such similar temperature dependences, the values of their ratios at a given temperature are not greatly affected

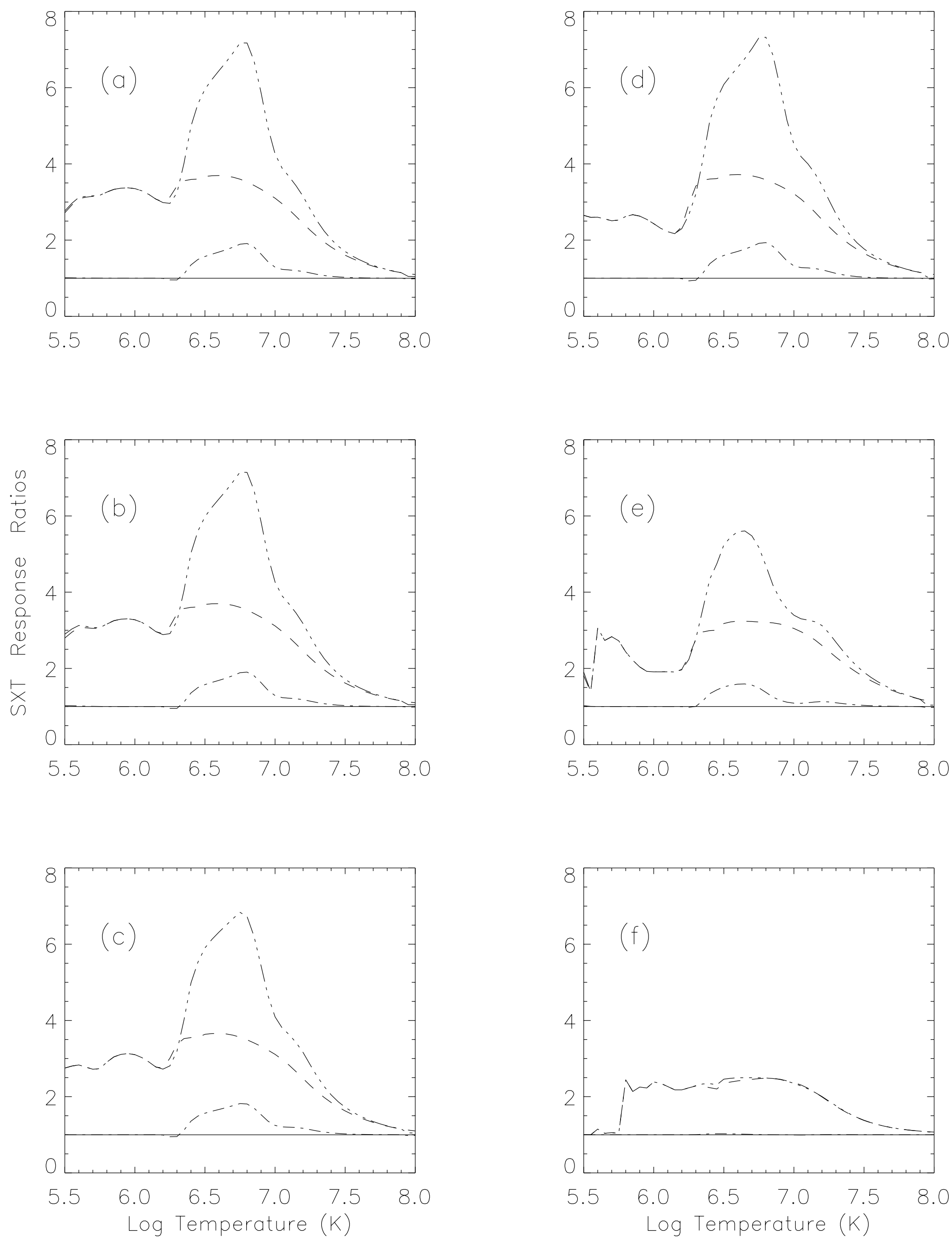

FIG. 3.—Several adjusted SXT filter responses normalized to the standard response (where the adopted coronal abundances of Meyer 1985 and the ionization fractions of Arnaud & Rothenflug 1985 are used to compute the synthetic solar spectrum which is folded through the SXT effective areas). The dashed curve shows the response generated using the Feldman (1992) abundances and Arnaud & Rothenflug (1985) ionization fractions, normalized to the standard response; the dot-dashed curve shows the response using the Meyer (1985) abundances and Arnaud & Raymond (1992) ionization fractions for iron, normalized to the standard response; and the triple-dot-dashed curve shows the response using the Feldman (1992) abundances and Arnaud & Raymond (1992) ionization fractions for iron, normalized to the standard response. The panels (*a*)–(*f*) correspond to the same SXT passbands as those in Figs. 1 and 2.

by changing the abundances or iron ionization fractions. (For example, the maximum change in the AlMgMn/thin-Al filter ratio for a factor of 4 increase in the iron abundance is $\sim$10%, which occurs at $\log T = 5.7$; the maximum change in the filter ratio due to substitution of the newer iron ionization fractions is $\sim$6%, which occurs at $\log T = 6.9$.) However, the color temperatures inferred from these ratios may still be altered significantly where the slope of the ratios with temperature is shallow. For example, the combined effect of replacing the iron ionization fractions and increasing the abundances by a factor of 4 over those in the SXT standard model yields increases in temperatures inferred from AlMgMn/thin-Al filter ratios of about 10% at $\log T = 6.5$, 20% at $\log T = 6.6$, and 30% at $\log T = 6.7$. The change in the inferred filter ratio temperatures can be even larger for ratios of thin filters combined with thick filters. For example, the thick-Al/thin-Al filter ratio temperatures increase by about 15% at $\log T = 6.5$, 30% at $\log T = 6.6$, and 40% at $\log T = 6.7$.

Moreover, the changes in emission measure (at a given temperature) are inversely proportional to the changes in the instrument response, which can be as much as a factor

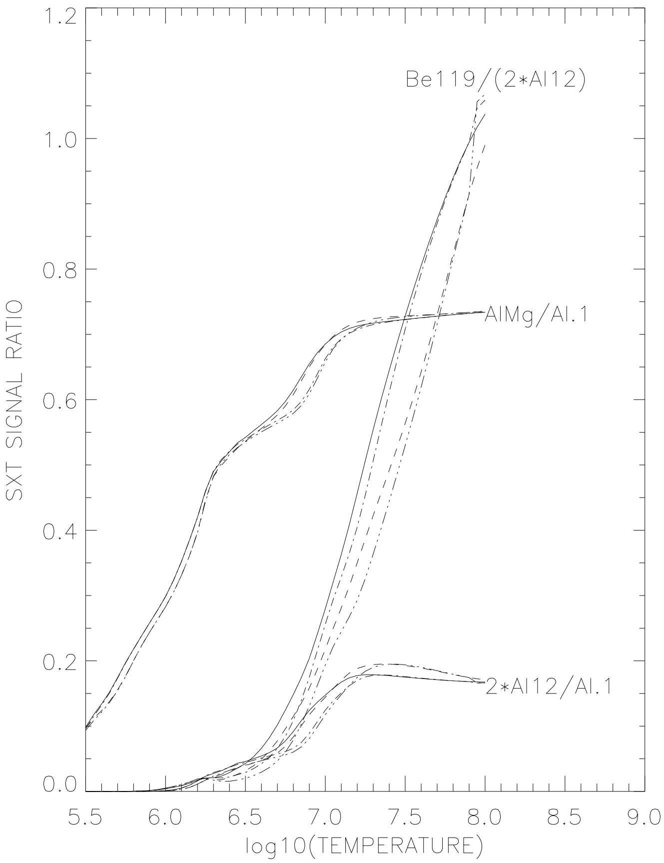

FIG. 4.—Ratios of the SXT filter responses as a function of temperature in the format of the figure in the *Yohkoh* Analysis Guide. The line type is the same as that used in Fig. 3. Note that even small changes to the ratio can result in significant changes to the temperature because the slopes of the curves are small.

of 7 as shown in Figure 3. Any model of the coronal plasma that requires the temperature or emission measure distribution could be severely affected by the choice of abundance normalization and/or ionization fraction used in the SXT analysis.

Given the sensitivity of the SXT filter responses to the change in elemental abundance normalization and iron ionization fractions, it is clear that a fair comparison between the SXT and SERTS data requires that the SXT response functions and the SERTS line emissivities be generated with the same set of elemental abundances and ionization fractions. For the emission measure distribution analysis presented in the next subsection, we adopted the hybrid elemental abundances listed in Table 1 (Schmelz & Fludra 1998) as discussed in § 3.1. Since the preferred values of the ionization fraction for iron are not clear, we did the multithermal analysis with both sets of calculations independently, to compare the results and see whether either did a better job of describing the combined SERTS and SXT data.

3.4. *Forward Folding*

Forward folding is a standard technique used to determine a plasma emission measure distribution as a function of temperature. It requires an initial input model which is folded through the spectral line emissivity functions or broadband responses. This produces a set of predicted intensities which are compared with the observed values. The emission measure distribution is then adjusted iteratively (and subjectively) to improve the agreement between the observed and predicted intensities while keeping the curve as smooth a function of temperature as possible. The process is repeated until, ideally, the predicted and observed intensities agree to within approximately ± 1–$2\ \sigma$ of the observed values.

The 23 SERTS spectral lines used in this analysis are listed in Table 2. The tabulated values are from Brosius et al. (1996). The emissivity functions for these lines, computed using information in the CHIANTI atomic physics database (version 1.01) compiled by Dere et al. (1997), are plotted as a function of temperature in Figure 5 for an electron density $n_e = 10^9$ cm^{-3}. The figure shows the good temperature coverage of the lines up to about log $T = 6.5$.

The dotted curve in Figure 6*a* shows the column emission measure distribution published by Brosius et al. (1996). The normalization of the curve was adjusted to conform to the definition of DEM as $n_e^2\, dl/dT$ with the assumption $n_{\rm H}/n_e = 0.8$ and with the Schmelz & Fludra (1998) abundances. This curve was used as the initial model for the forward-folding program. The program generated a set of predicted intensities for the 23 SERTS spectral lines listed in Table 2 as well as the three SXT broadband filters (thin Al, AlMgMn, and thick Al) for which cotemporal data were available. The predicted/observed ratios were within ± 1–$2\ \sigma$ for most of the SERTS lines but were greater than $+5\ \sigma$ for the SXT filter data if the total uncertainties on the measured intensities are taken to be 20% (see § 4.1). Since SXT is more sensitive to high-temperature (log $T > 6.5$) plasma than SERTS, these results suggested that the high-temperature

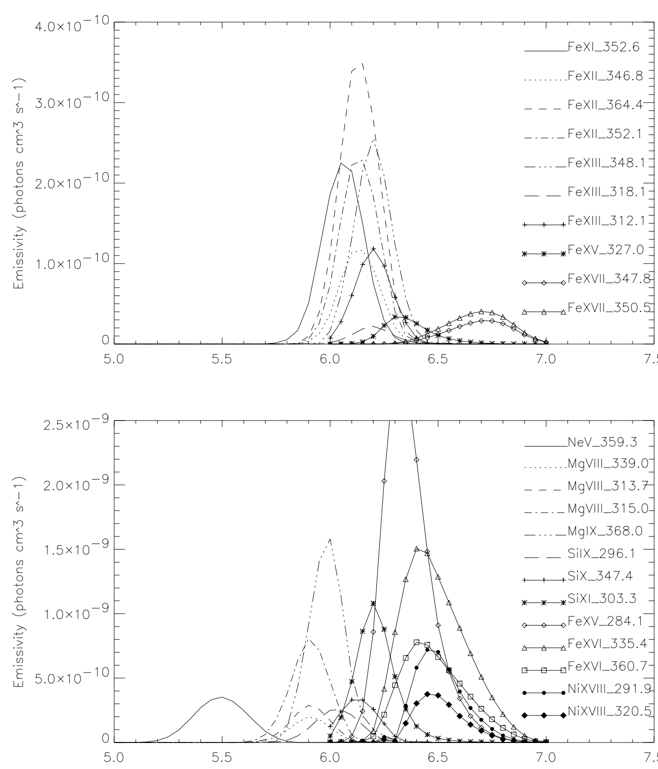

FIG. 5.—Emissivity functions for the 23 SERTS lines computed using information in the CHIANTI atomic physics database compiled by Dere et al. (1997) for an assumed electron density of 10^9 cm^{-3}. The emissivities of the two Fe XVII lines which peak at about log $T = 6.7$ were multiplied by a factor of 10 to make them visible on this scale.

TABLE 2

PROPERTIES OF SERTS SPECTRAL LINES

Number	Ion	λ (Å)	log T_{max}	Intensity	Uncertainty	Transition
1	Ne V	359.383	5.50	2.51E+01	5.29E+00	$2s^2 2p^2\ ^3P_2$–$2s^2 p^3\ ^3S_1$
2	Mg VIII	339.014	5.90	6.42E+01	8.48E+00	$2s^2 2p\ ^2P_{3/2}$–$2s2p^2\ ^2S_{1/2}$
3	Mg VIII	313.744	5.90	6.78E+01	1.05E+01	$2s^2 2p\ ^2P_{1/2}$–$2s2p^2\ ^2P_{1/2}$
4	Mg VIII	315.029	5.90	2.32E+02	2.70E+01	$2s^2 2p\ ^2P_{3/2}$–$2s2p^2\ ^2P_{3/2}$
5	Mg IX	368.093	6.00	9.43E+02	1.10E+02	$2s^2\ ^1S_0$–$2s2p\ ^1P_1$
6	Fe XI	352.699	6.05	1.77E+02	2.02E+01	$3s^2 3p^4\ ^3P_2$–$3s3p^5\ ^3P_2$
7	Si IX	296.108	6.05	2.70E+02	4.10E+01	$2s^2 2p^2\ ^3P_2$–$2s2p^3\ ^3P_2$
8	Fe XII	346.867	6.15	1.15E+02	1.40E+01	$3s^2 3p^3\ ^4S_{3/2}$–$3s3p^4\ ^4P_0$
9	Fe XII	364.494	6.15	2.57E+02	2.95E+01	$3s^2 3p^3\ ^4S_{3/2}$–$3s3p^4\ ^4P_2$
10	Fe XII	352.131	6.15	1.90E+02	2.21E+01	$3s^2 3p^3\ ^4S_{3/2}$–$3s3p^4\ ^4P_1$
11	Si X	347.421	6.15	2.86E+02	3.26E+01	$2s^2 2p\ ^2P_{1/2}$–$2s2p^2\ ^2D_{3/2}$
12	Fe XIII	348.199	6.20	2.10E+02	2.43E+01	$3s^2 3p^2\ ^3P_0$–$3s3p^3\ ^3D_1$
13	Fe XIII	318.121	6.20	8.59E+01	1.26E+01	$3s^2 3p^2\ ^1D_2$–$3s3p^3\ ^1D_2$
14	Fe XIII	312.171	6.20	1.05E+02	1.65E+01	$3s^2 3p^2\ ^3P_1$–$3s3p^3\ ^3P_1$
15	Si XI	303.317	6.20	2.88E+03	3.26E+02	$2s^2\ ^1S_0$–$2s2p\ ^1P_1$
16	Fe XV	284.135	6.30	5.78E+03	6.51E+02	$3s^2\ ^1S_0$–$3s3p\ ^1P_1$
17	Fe XV	327.045	6.30	5.22E+01	6.64E+00	$3s3p\ ^3P_2$–$3p^2\ ^1D_2$
18	Fe XVI	335.418	6.40	4.09E+03	4.70E+02	$3s\ ^2S_{1/2}$–$3p\ ^2P_{3/2}$
19	Fe XVI	360.782	6.40	2.04E+03	2.32E+02	$3s\ ^2S_{1/2}$–$3p\ ^2P_{1/2}$
20	Ni XVIII	291.961	6.45	1.23E+02	2.87E+01	$3s\ ^2S_{1/2}$–$3p\ ^2P_{3/2}$
21	Ni XVIII	320.568	6.45	4.66E+01	6.59E+00	$3s\ ^2S_{1/2}$–$3p\ ^2P_{1/2}$
22	Fe XVII	347.823	6.70	9.17E+00	3.73E+00	$2p^5 3s\ ^3P_1$–$2p^5 3p\ ^1D_2$
23	Fe XVII	350.521	6.70	1.70E+01	6.43E+00	$2p^5 3s\ ^3P_2$–$2p^5 3p\ ^3D_3$

NOTE.—Intensities are in units of ergs $cm^{-2}\ s^{-1}\ sr^{-1}$.

portion of the Brosius et al. (1996) DEM curve needed to be modified using the information provided by SXT.

The initial distribution was changed by small, iterative steps to bring the predicted SXT data points to within ± 1–$2\ \sigma$ of the observed values. The solid curve in Figure 6*a* shows the DEM curve that minimized the difference between the predicted and observed intensities. The associated error ratios are shown as crosses in Figure 6*b*. Position numbers for the SERTS lines (1–23) correspond to the listings in Table 2 while numbers 24, 25, and 26 represent the three SXT filters—thin Al, AlMgMn, and thick Al. This curve was chosen to optimize the fit of the intensities recorded in the three SXT channels since this instrument has the more reliable high-temperature response. As a result the predicted intensities for many of the SERTS lines are much lower than their observed counterparts. The Fe XIII line at 318.12 Å (position number 13) is one of the few lines here that is sensitive to density. This line does not affect our main results, and we postpone a detailed discussion about possible density effects to a future paper. The low values for the Fe XV, Fe XVI, Ni XVIII, and Fe XVII lines (position numbers 16–23) are a much bigger problem since these are the lines whose peak formation temperatures significantly overlap with the SXT filter responses. All of these lines are insensitive to density in the range appropriate for active region loops. We investigate the possible sources of this discrepancy in the next section.

4. DISCUSSION

The solid DEM curve in Figure 6*a* is comparable to the dotted curve for log $T < 6.5$; however, it is missing the high-temperature peak because the SXT data are not compatible with a significant amount of emission from plasma at log $T > 6.5$. The DEM curve cannot be made consistent with both the SXT data and the SERTS higher temperature line intensities as given in Table 2. We consider the two most likely reasons for this discrepancy: (1) a problem with either the atomic physics or the observations of the higher temperature SERTS lines and/or (2) a relative calibration discrepancy between the two instruments of a factor of 2–4. We then discuss the physical implications for the adjusted DEM curve.

4.1. *Possible Sources of Uncertainty*

All of the lines with peak formation temperatures at log $T = 6.3$ or higher have predicted values that are too low based on the DEM curve optimized for the SXT data. The most discrepant lines are those of Fe XVII (positions 22 and 23 in Fig. 6*b*) at 347.8 and 350.5 Å. These lines are extremely weak in all of the SERTS spectra, with relatively large measurement uncertainties. The peak formation temperature of Fe XVII differs significantly depending on which ionization fractions are used, but repeating the analysis with the Arnaud & Rothenflug (1985) ionization balance calculations for iron in both the SERTS emissivities and SXT response functions did not improve the results. A new study by Bhatia & Kastner (1999) shows that these two lines should not be affected by opacity at the temperatures and densities appropriate for active regions. According to calculations using the CHIANTI database, there is a group of Si X lines near the 347.8 Å line which could overwhelm the Fe XVII contribution to the flux, but there are no known lines that could contribute significantly to the observed line at 350.5 Å. Hence, there is no obvious reason which satisfactorily explains why the ratios of predicted-to-observed intensity would be so low for these lines.

The Ni XVIII lines at 292.0 and 320.6 Å (lines 20 and 21) are also weak in the SERTS spectra, although stronger than the Fe XVII lines discussed above. Preliminary calculations suggest that both lines are optically thin under coronal con-

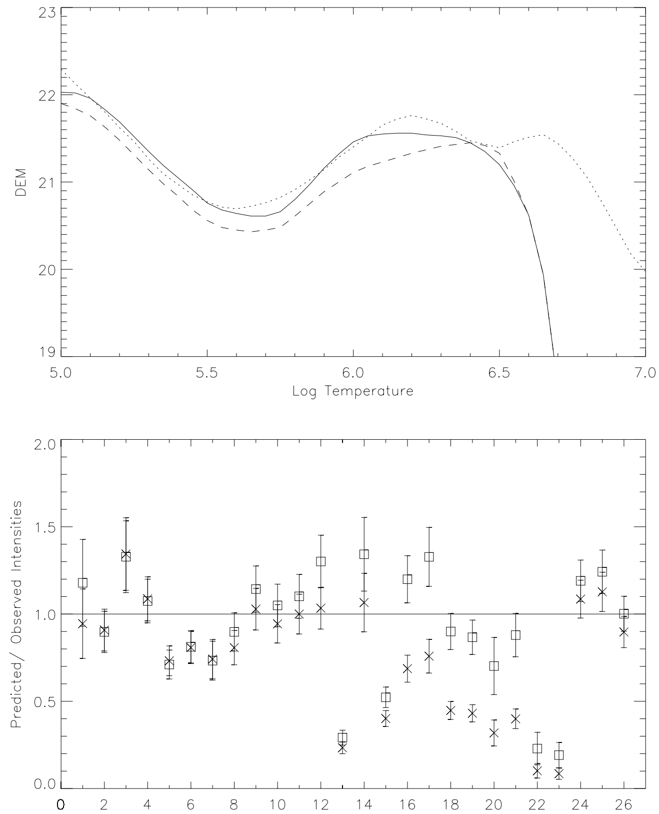

FIG. 6.—(*a*) The dotted curve represents the DEM distribution of Brosius et al. (1996), adjusted to conform to the definition of DEM as $n_e^2\, dl/dT$ with the abundance normalization of Schmelz & Fludra (1998) and the assumption that $n_{\rm H}/n_e = 0.8$. The ionization fractions of Arnaud & Raymond (1992) are used for iron. The solid curve represents the DEM distribution that optimizes the fit of the intensities recorded in the three available SXT channels. It assumes an instrumental cross-calibration factor of 1 (i.e., that SXT and SERTS are perfectly cross calibrated). The dashed curve represents the best fit to the data assuming an instrumental cross-calibration factor of 2. (*b*) The predicted-to-observed intensity ratio on a linear scale for the 23 spectral lines listed in Table 2 as well as the SXT broadband data for the thin-Al, AlMgMn, and thick-Al filters (position numbers 24, 25, and 26). The error points denoted by crosses and squares are associated with the solid curve and the dashed curve, respectively.

ditions. A search of the CHIANTI database finds no lines that would be expected to contribute significantly to the measured intensity of the 292.0 Å line, but there is a nearby Mg VII line that could contaminate the line at 320.6 Å. However, the n_e-insensitive ratio of these nickel lines is as expected. If these nickel lines were the only two lines for which the observed and predicted intensities differed significantly, we might be tempted to assume that the nickel abundance of the active region plasma is somewhat higher than expected. There are excellent examples of abundance variability in the literature which do not follow the strict FIP formula. But since the iron lines on both the high- and low-temperature sides of the nickel lines are also problematic, adjusting the Ni/Fe abundance is not the solution.

The observed intensities are also substantially higher than those predicted for the Fe XVI lines at 335.4 and 360.8 Å (lines 18 and 19, with log $T = 6.4$) and the Fe XV lines at 284.1 and 327.0 Å (lines 16 and 17, log $T = 6.3$). All four lines are strong and, based on the CHIANTI database, should have no significant blends. Preliminary analysis suggests they are optically thin under coronal conditions. Changing the iron abundance will not help because the SXT broadband responses would be affected almost as strongly as the SERTS emission lines.

It is difficult to attribute the discrepancies between the observed and predicted intensities for all the lines of Fe XV, Fe XVI, Fe XVII, and Ni XVIII to blending, optical depth effects, or abundance variations. The simplest alternative explanation is that these discrepancies are manifestations of instrumental uncertainties on the absolute intensity measurements. The SXT absolute intensity in 1993 after the failure of the front filter is thought to be good to 20% (L. Acton 1999, private communication). The uncertainty on the SERTS absolute intensity calibration is a factor ~ 2, meaning that the SERTS line intensities could be divided by a factor of 2 and still remain within the measurement uncertainty. Therefore, we systematically divided the SERTS intensities given in Table 2 by a factor of 2 and repeated the DEM computations described above. The results are plotted as the dashed line on Figure 6*a*, and the associated errors are shown as the squares in Figure 6*b*. Note that this brings the Fe XV and Fe XVI lines into agreement with the SXT data. The Ni XVIII lines can be adjusted by changing the Ni elemental abundance slightly. The Fe XVII lines, however, are still off by more than a factor of 2 and would require an unrealistically large cross-calibration factor to bring them into agreement. Similar results were obtained using Arnaud & Rothenflug (1985) ionization fractions.

Both the SERTS and SXT data were examined in detail for transient, localized brightenings that might affect the Fe XVII spectral lines disproportionately since they are the hottest SERTS lines used in this analysis. In a detailed discussion of the SERTS data, Brosius et al. (1997) describe the consistency of the data from this quiescent active region and find the intensity of the Fe XVII lines to be consistent throughout the data used here. Further, any transient brightening in Fe XVII emission in the SERTS data should have been reflected in the series of SXT images taken just before and during the SERTS flight, as discussed in § 2.2; no such signature was found. Since the discrepancy cannot be attributed to statistical or systematic uncertainties, we are left with no other option than to suggest that the atomic physics for these lines be reexamined.

4.2. *Physical Implications*

Removing the high-T component from the original DEM curve (because of its inconsistency with the SXT data) reduces the thermal energy content $E_{\rm th}/V \sim 2.7 n_e kT$ of the active region emission volume V, by about a factor of 2, for whatever absolute abundance normalization or absolute SERTS calibration is chosen. (Here k is the usual Boltzmann constant and it was assumed $n_p \sim 0.8 n_e$.) However, it reduces the heating requirement by about a factor of 5.

For Meyer FIP-biased adopted coronal abundances, the radiative loss function calculated by Cook et al. (1989) can be evaluated near log $T = 6.5$ as

$$P_{\rm rad} \sim 1.5 \times 10^{-23} n_e n_{\rm H} \sim 1.2 \times 10^{-3} n_{10}^2 \ {\rm ergs\ s^{-1}\ cm^{-3}} , \quad (1)$$

where $n_{\rm H}$ is the number density of H (taken to be $\sim 0.8 n_e$) and n_{10} is n_e in units of 10^{10} cm^{-3}. Then the radiative cooling time,

$$t_{\rm rad} = \frac{E_{\rm th}/V}{P_{\rm rad}} \sim 3 \times 10^3 T_6 n_{10}^{-1} \ {\rm s} , \quad (2)$$

where T_6 is the temperature in MK, becomes $t_{\rm rad} \sim 3 \times 10^4$ s for $n_{10} = 0.3$ (a typical active region density). The equivalent value for $P_{\rm rad}$ at $T_6 = 3$ calculated using Arnaud & Raymond (1992) ionization fractions (J. Raymond 1999, private communication; see Fig. 3.12 of Golub & Pasachoff 1997) is about twice as large as that of Cook et al. (1989), so the radiative cooling timescale would be about half as long.

The conductive cooling timescale for active region coronal plasma in volume $V = L \times A_{\rm loop}$ for a loop of half-length L and (constant) cross-sectional area $A_{\rm loop}$ was estimated by Saba & Strong (1991) to be

$$t_{\rm cond} \sim 10^4 L_9^2 n_{10} T_6^{-2.5} \text{ s} , \tag{3}$$

where L_9 is the loop half-length in units of 10^9 cm; for $2L_9 = 10$, $n_{10} \sim 0.3$, and $T = 3$ MK, this yields $\sim 5 \times 10^3$ s. For coronal loops of the same length and density, the conductive cooling rate is about 15 times slower at 1 MK and about 5 times faster at 6 MK than at 3 MK. The radiative cooling rate is about half as fast at 6 MK as at 3 MK and about 10–50 times faster at 1 MK than at 3 MK (depending on which calculation of $P_{\rm rad}$ is used). The actual values for the cooling timescales depend on the specific values of the input parameters—in particular, n_e, L, and the coronal abundance normalization. However, we can estimate that, for the hybrid abundances, active region loops at 3 MK will cool in a few times 10^3 s (with radiation and conduction competitive), while the 6 MK loops will cool about 5 times faster (primarily by conduction) and the 1 MK loops will cool 5–10 times faster (primarily by radiation). This may explain why temperatures of stable active region loops measured at X-ray wavelengths by instruments such as the *Solar Maximum Mission* Flat Crystal Spectrometer were found to be typically about 3 MK (Schmelz et al. 1996). Thus, the adjustments to the DEM curve (principally, removal of emission measure above log $T = 6.5$, but also smaller decrements at log $T = 6.0$–6.3) were driven by the data but appear to be supported also on physical grounds.

As pointed out by Cook et al. (1989), the shape of the radiative loss function at coronal temperatures is significantly altered when coronal elemental abundances are used in place of photospheric abundances for the emitting plasma. Golub & Pasachoff (1997) note that the various local peaks in the radiative loss function at coronal temperatures come largely "from a few of the most important spectral lines emitted by a few stages of ionization of a small number of individual elements." For a FIP-biased composition, the radiative cooling of the corona comes primarily from line emission from iron ions and other metals; thus, for a given emission measure, the higher the enhancement of iron and other low-FIP element abundances over their photospheric values, the higher the radiative cooling rate will be in the temperature regime log $T \sim 6.0$–6.6. If all the other required input parameters (n_e, DEM, loop size, shape, and filling factor) were known from simultaneous high-resolution spectroscopic and imaging data, then observed cooling times might offer an important new constraint on the absolute abundance normalization at least for the prime radiating ions such as iron. Although there are a number of studies of relative abundances of heavy elements in the active corona, apart from flare conditions (where line-to-continuum analysis is possible), definitive spectroscopic measurements of heavy element abundances relative to hydrogen remain elusive.

5. CONCLUSIONS

This investigation compared and combined information on the emission measure distribution with temperature for a quiescent active region, AR 7563, using a forward-folding technique on simultaneous SXT broadband filter images and SERTS high-resolution EUV spectra. We exploited the complementary nature of the SXT and SERTS data to achieve three interdependent goals: (1) quantification of some of the important uncertainties inherent in the use of the individual data sets, (2) an improved calibration of the relative SERTS and SXT responses, and (3) a self-consistent multithermal description of the active region plasma. Our results are summarized below.

Although it is generally understood that emissivities of spectral lines such as those observed with SERTS will depend greatly on the set of elemental abundances assumed and the ionization fraction calculations used, it has often been unrecognized that broadband filter response functions such as those for SXT are also sensitive to these details of the solar spectrum that is folded through the instrument effective area.

The sensitivity of the SXT filter response functions to both the absolute elemental abundances (primarily for iron) and the iron ionization fractions could have a major impact on many routine analyses of SXT data. The dominant contribution of iron emission lines in the SXT thin filter bandpass yields about a factor of 2 difference in response at ~ 6 MK when the default iron ionization fractions (from calculations of Arnaud & Rothenflug 1985) are replaced with those of the newer ionization balance calculation of Arnaud & Raymond (1992). At plasma temperatures of 2–5 MK, the emission measures derived from the thin filter count rates scale roughly inversely with the assumed Fe/H normalization; the magnitude of the effect is not constant with temperature, dropping by about a factor of 2 at flare temperatures (~ 25 MK).

Color temperatures obtained from ratios of various combinations of SXT low-energy filters can be affected significantly (e.g., 10%–30% at log $T = 6.5$–6.7) by changing abundances or iron ionization fractions even though the response curves of the low-energy filters have similar temperature dependence. This is because of the shallow gradient of the ratio as a function of temperature, that is, a small change in filter ratio corresponds to a larger change in temperature. The effect of changing abundances and iron ionic fractions on color temperatures from ratios of thin filters combined with thick filters, or of the thick Al with the Be filter, can be even larger (e.g., 15%–40% at log $T = 6.5$–6.7 for the thick-Al/thin-Al filter combination and 50%–60% for the Be/thick-Al filter combination).

We found that the relative calibration between the SERTS and the SXT instruments must be adjusted by a factor of 2. This is consistent with the absolute measurement uncertainty of the 1993 SERTS flight (Brosius, Davila, & Thomas 1998). Using a forward-folding procedure which combines the SXT intensities with the published SERTS line intensities divided by a factor of 2 yielded acceptable joint emission measure distributions. Our present analysis cannot determine whether the Arnaud & Rothenflug (1985) or Arnaud & Raymond (1992) ionization fractions better describe the joint data set, nor can it choose the preferred absolute coronal abundance normalization. However, it does demonstrate (1) the strong need that all atomic physics assumptions be the same for both data sets when SXT broadband data are compared with spectral line data and (2) the range of results possible when the absolute abundances and iron ionization fractions are uncertain.

We revised the DEM curve of Brosius et al. (1996) to be consistent simultaneously with both SERTS and SXT observations, within their respective measurement uncertainties. The major change was a sharp drop in the DEM distribution starting at about log $T = 6.5$, which effectively reduces the thermal energy content of the region by about a factor of 2 and the heating requirements by about a factor of 5. There was also a slight enhancement of emission measure around log $T = 6.5$ relative to plasma near log $T = 6.0$; this also reduces the heating requirement somewhat because more heating would be required to offset radiative cooling near log $T = 6.0$. The SERTS data alone do not contain an effective high-temperature constraint for active region plasma, and so DEM results from SERTS data alone should be used with considerable caution. This caveat also applies to the analysis of data obtained solely from an instrument such as the Coronal Diagnostic Spectrometer (CDS) on *SOHO* which has a similar wavelength range.

There are several lines in the SERTS wavelength range which were not consistent with our analysis results. We plan a more detailed investigation of the density sensitivity of the Fe XIII line at 318.1 Å and other lines in the SERTS wavelength range in a future paper. The differences between the observed and predicted values of the two Fe XVII lines at 347.8 and 350.5 Å could not be reconciled with any adjustment of the iron elemental abundance or ionization fraction or relative calibration between the SERTS and SXT instruments. We suggest that the atomic physics for these lines be investigated more thoroughly.

We plan to make a similar analysis of coordinated data from the 1997 November 18 SERTS flight, where simultaneous observations are available not only from SXT but also from CDS. Since one of the purposes of that flight was to obtain a reliable cross calibration between SERTS and CDS, SERTS was absolutely calibrated in the same facility used to calibrate CDS prior to the *SOHO* launch. The absolute intensity measurement uncertainty is much less than the factor ~ 2 from previous flights. A more reliable SERTS/SXT relative calibration will substantially reduce one of the important uncertainties in the analysis method used here and should significantly improve the constraints of a joint multithermal analysis.

This work was supported by the *Yohkoh* Guest Investigator Program through NASA contract NASW-5052. Solar physics research at the University of Memphis is supported through NASA grant NAG 5-7197. J. W. B. acknowledges NASA support through contract NASW-5020. K. T. S. acknowledges support by the Lockheed Martin Independent Research and Development Program. The SERTS program receives NASA support through RTOP grants from the Solar Physics Office of NASA's Space Physics Division. We are grateful to Jim Lemen and Phil Shirts of the Lockheed Martin Solar and Astrophysics Lab for updating the SXT analysis software to account for different elemental abundances and iron ionization fractions. John Raymond kindly provided his calculations of the radiative loss function for various elemental abundance sets. It is a pleasure to thank University of Memphis physics students Richie Scopes, Rick Edwards, and Ben Schoepke for assistance with data analysis.

REFERENCES

Arnaud, M., & Raymond, J. 1992, ApJ, 398, 394

Arnaud, M., & Rothenflug, R. 1985, ApJS, 60, 425

Bhatia, A. K., & Kastner, S. O. 1999, ApJ, 516, 482

Brosius, J. W., Davila, J. M., & Thomas, R. J. 1998, ApJS, 119, 255

Brosius, J. W., Davila, J. M., Thomas, R. J., & Monsignori-Fossi, B. C. 1996, ApJS, 106, 143

Brosius, J. W., Davila, J. M., Thomas, R. J., Saba, J. L. R., Hara, H., & Monsignori-Fossi, B. C. 1997, ApJ, 477, 969

Cook, J. W., Cheng, C.-C., Jacobs, V. L., & Antiochos, S. K. 1989, ApJ, 338, 1176

Dere, K. P., Landi, E., Mason, H. E., Monsignori-Fossi, B. C., & Young, P. R. 1997, A&AS, 125, 149

Feldman, U. 1992, Phys. Scr., 46, 202

Golub, L., & Pasachoff, J. M. 1997, The Solar Corona (Cambridge: Cambridge Univ. Press)

Harrison, R. A. & Thompson, A. M. 1991, Rutherford Appleton Laboratory Publications, RAL-91-092

Meyer, J.-P. 1985, ApJS, 57, 173

Morrison, M. 1994, *Yohkoh* Analysis Guide, LMSC-P098510

Neupert, W. M., Epstein, G. L., Thomas, R. J., & Thompson, W. T. 1992, Sol. Phys., 137, 87

Saba, J. L. R., & Strong, K. T. 1991, ApJ, 375, 789

Schmelz, J. T., & Fludra, A. 1998, *EOS*, 79, 17, S258

Schmelz, J. T., Holman, G. D., Brosius, J. W., & Willson, R. F. 1994, ApJ, 434, 786

Schmelz, J. T., Saba, J. L. R., Ghosh, D., & Strong, K. T. 1996, ApJ, 473, 519

Tsuneta, S., et al. 1991, Sol. Phys., 136, 37